A Four Port Ultra-Wideband MIMO Antenna with Windmill Shaped Decoupling Structure and Olympic Five Ring Patch

Chang Li[1], Zhonggen Wang[1, *], Wenyan Nie[2], and Ming Yang[3]

[1]*School of Electrical and Information Engineering, Anhui University of Science and Technology, Huainan 232001, China*
[2]*School of Mechanical and Electrical Engineering, Huainan Normal University, Huainan 232001, China*
[3]*School of Electrical and Communications Engineering, West Anhui University, Lu'an 237012, China*

ABSTRACT: In this paper, a compact and highly isolated ultra-wideband (UWB) four-port multiple-input-multiple-output (MIMO) antenna design is proposed, employing coplanar waveguide (CPW) feeding technology. The antenna system is meticulously arranged on a 0.787 mm thick RO5880 substrate, occupying a footprint of $56 \, \text{mm} \times 56 \, \text{mm}$ ($1.5\lambda \times 1.5\lambda$). The design comprises four identically modified antenna elements orthogonally positioned. Each element consists of an Olympic ring-shaped radiating patch within a slotted frame and two fin-shaped ground planes with E-shaped slots. Additionally, a windmill-like decoupling structure formed by rotating stubs is introduced to further enhance performance. This layout not only optimizes the isolation between antenna elements but also enhances overall performance through its unique structural design, ensuring better signal stability and wider bandwidth. The antenna system achieves an impedance bandwidth ranging from 3.65 GHz to 13.95 GHz. A thorough examination was performed on various essential MIMO performance indicators, such as envelope correlation coefficient (ECC) and total active reflection coefficient (TARC). The findings reveal that the antenna exhibits outstanding performance in these aspects, with an ECC value under 0.0012 and a TARC value under -30 dB. These results underscore the considerable potential and high performance of the proposed UWB-MIMO antenna for diverse UWB applications.

1. INTRODUCTION

UWB technology is characterized by fast transmission and low energy consumption. When being combined with MIMO technology, it enhances bandwidth, data rates, and short-range wireless communication while reducing multipath fading. It is widely applied to positioning, smart wearables, internet of things (IoT), and other fields [1]. In the design of UWB-MIMO antennas, attention should center on elements like compact form factor, operational frequency range, and signal isolation. Thus far, scholars have investigated multiple strategies to widen the bandwidth and boost the isolation performance of compact UWB-MIMO antennas. These approaches encompass the use of L-shaped ground stubs, T-shaped stubs, fence-like decoupling structures, electromagnetic bandgap (EBG) configurations, and defected ground structures (DGSs). Each method aims to optimize antenna efficiency and functionality for enhanced performance in various applications [2–6], metamaterials and various configuration techniques [7–10]. The utilization of these methods is geared towards refining antenna performance and enhancing the overall efficiency of the system.

The antenna design in [11] employs a fin-shaped ground plane and framework, initially demonstrating resonance bands at 5 GHz to 6 GHz and 9 GHz to 11 GHz. Introducing the framework and hollow enclosure achieves dual-mode resonance in the 3 GHz to 5 GHz range and above 9 GHz. Incorporating

a ring structure adjusts the resonance bands to 3.3 GHz to 8.5 GHz, significantly enhancing bandwidth and frequency response. This indicates that incorporating ring structures in similar configurations can optimize bandwidth, thus effectively improving antenna performance in analogous designs. The antenna design in [12] incorporates a curved decoupler that achieves over 18 dB of isolation in the 8 GHz to 12 GHz band, suitable for most of the UWB spectrum. Utilizing four rotated curved stubs, this design enhances the isolation between antenna elements. This efficient and straightforward decoupler not only broadens the impedance bandwidth but also improves overall system performance. Therefore, when designing antenna decoupling structures, considering rotated curved stubs as design elements can achieve similar performance enhancements. In [13, 14], a compact four-port MIMO antenna utilizing defected ground plane techniques for selective bandwidth and port isolation, and a design employing an inverted L-shaped defected ground plane to broaden bandwidth and enhance port-to-port isolation are presented, respectively. Both studies indicate that introducing innovative isolation structures or incorporating appropriate slots on the ground plane can optimize port isolation at lower frequencies and overall bandwidth performance, thereby enhancing the antenna system's effectiveness across the entire operational frequency band. Refs. [15–18] propose various antenna decoupling methods: Metasurface technology provides over 25 dB isolation in the 2.5 GHz to 2.7 GHz and 3.4 GHz to 3.6 GHz bands but increases size and integration complexity; EBG structures enhance the isolation by

TABLE 1. Dimensions of the proposed MIMO antenna structure.

| parameters	L_1	L_2	L_3	L_4	L_5	M_1	M_2	M_3	M_4
Value (mm)	56	14.2	14.9	0.1	0.2	9	2.5	2.12	0.605
parameters	M_5	M_6	W_1	W_2	W_3	W_4	W_5	W_6	W_7
Value (mm)	2	0.5	56	7.7	12	0.4	4.5	11.05	20.54
parameters	W_8	W_9	W_{10}	W_{11}	R_1	R_2	D_1		
Value (mm)	11	12.56	3.5	2.7	1	1.8	1		

10 dB for dual-port UWB-MIMO antennas within the 3.1 GHz to 13.5 GHz range, although their complex geometries raise costs and manufacturing difficulties; grounded multi-branch T-shaped stubs achieve effective isolation in specific frequency bands and further performance improvements through additional techniques; fence-type decoupling structures boost isolation in two-element MIMO antenna systems and demonstrate potential for novel designs. These studies highlight the critical importance of innovative structures in enhancing isolation and overall performance of antenna systems. In [19], a fractal sunflower-shaped antenna measuring 32.42 mm × 64.3 mm with three notches is introduced, achieving filtering through the incorporation of a C-shaped complementary split-ring resonator (CSRR) slot into the feed line. This design leverages the self-similarity of fractals to increase the current path length, thereby expanding the impedance bandwidth. By adopting this approach, the introduction of structures similar to Olympic ring-shaped patches and additional fractal notches or substructures can enhance UWB coverage or multi-band characteristics without increasing the antenna size, while maintaining its compactness and functionality.

This paper introduces a MIMO antenna design aimed at achieving ultra-wide bandwidth and high isolation. The key advantages of this design include full coverage of the UWB frequency band (3.65 GHz to 13.95 GHz), inter-port isolation exceeding 21.7 dB with an ECC less than 0.0012, a compact structure (56 mm × 56 mm), and efficient radiation performance (87% to 93%). However, it also faces several challenges, such as the lack of narrowband notch functionality, the need for further miniaturization, higher manufacturing costs due to the use of windmill-shaped structures and E-shaped slots, potential performance fluctuations caused by human contact in handheld scenarios, and the necessity to optimize decoupling structures when scaling up to large-scale MIMO configurations.

2. PROPOSED ANTENNA DESIGN

2.1. Structure of MIMO Antenna

Figure 1 illustrates the proposed MIMO antenna geometry, employing CPW feeding technology due to its advantages of low loss, coplanar structure, and ease of fabrication. Four radiating elements are orthogonally arranged with respect to the ground plane and printed on a 0.787 mm thick RO5880 substrate (relative permittivity of 2.2 and loss tangent of 0.0009). The design incorporates a five-ring structured radiator with slotted frames, fin-shaped ground planes with E-shaped slots, and a windmill-
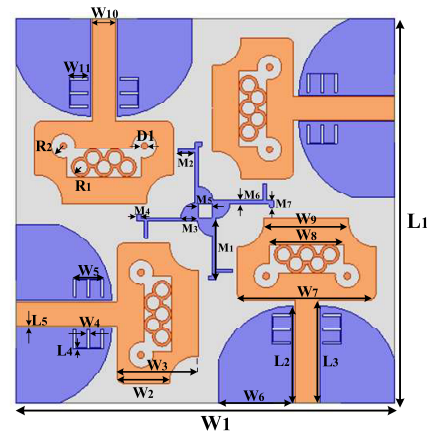
FIGURE 1. UWB-MIMO antenna structure.

like decoupling structure formed by rotated stubs, achieving UWB performance and high isolation. This design integrates the advantages of monopole antennas (with five-ring patches as the main radiating element) and slot antennas (with slotted frames and E-shaped slots), where the monopole mode dominates low-frequency radiation, and the slot mode enhances high-frequency radiation, collectively achieving wideband coverage. It also addresses the issue of strong coupling between elements in traditional MIMO antennas through decoupling structures. Table 1 summarizes the final optimized parameters.

Figure 2 illustrates various structures of antennas and their corresponding equivalent circuits, where the resonant characteristics of these structures are determined by their parameters, forming specific band equivalent circuits to achieve resonant radiation. The resonance of the microstrip line framework (Circuit 1) depends on its length, width, and distance from the ground plane, which is equivalent to a parallel combination of inductor L_1 and capacitor C_1. By adjusting dimensions such as L_2 and W_2, an equivalent circuit for the 4.3 GHz band can be generated. The performance of the E-shaped slot structure (Circuit 2) is influenced by slot width, slot length, and position, equivalent to a parallel of inductor L_2 and capacitor C_2. Optimizing parameters like L_4 and slot spacing can generate an equivalent circuit for the 10.9 GHz band. The resonant condition of the Olympic ring structure (Circuit 3) is controlled by ring size, slot position, and thickness, equivalent to a parallel of inductor L_3 and capacitor C_3. The proper design of parameters such as R_1 and R_2 can produce an equivalent circuit for the 12.2 GHz band. Through specific parameter adjustments and optimizations, each structure achieves effective resonant radiation within its respective frequency band.
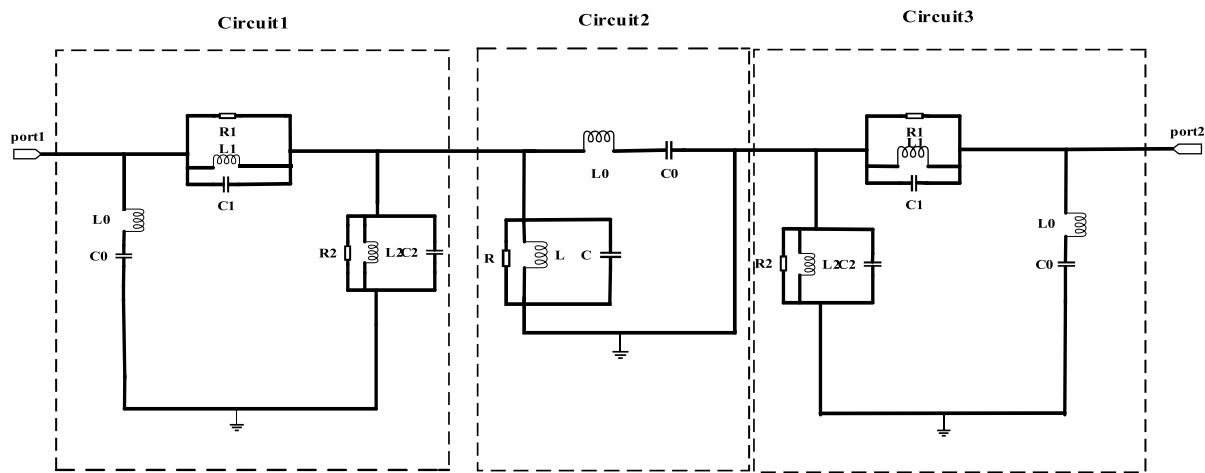
FIGURE 2. Equivalent circuit of the proposed two-port MIMO antenna.

2.2. Design Evolution Stages of the MIMO Antenna

To introduce additional inductive effects and adjust resonance frequencies by altering current paths, the design incorporates radiators with rectangular slots. Simultaneously, the slot structures help suppress surface wave propagation, reduce energy loss, and enhance efficiency. The five-ring structure creates composite radiating elements using multiple annular slots, which, under feed signal excitation, stimulate multimode resonances. Each ring corresponds to different resonance frequencies, effectively broadening the impedance bandwidth. For instance, at the 12.2 GHz band, the optimized five-ring structure achieves uniform current distribution through precise capacitance and inductance matching, efficiently exciting high-frequency resonance. Owing to these advantages, this structure was selected for the radiator design. To elaborate on the proposed antenna design methodology, Figure 3 illustrates the design evolution of four models: the initial model, frame-adjusted model, floor-slotted model, and isolation-structure-added model. Figure 4 compares the S-parameters of MIMO antennas with four different configurations. By altering the shape of the antenna patches, slitting the floor, and introducing isolation structures, the antenna achieves a wider bandwidth and outstanding interference resistance performance.

Firstly, the antenna in Figure 3(a) uses traditional CPW feeding technology. It achieves good isolation ($S_{13} > -17$ dB at low frequencies) and wide bandwidth through orthogonal layout, even without extra isolation structures. However, to further improve isolation, future optimizations will include dedicated isolation structures. Among them, the loop patch serves as a critical radiation element for the X band, whereas the rectangular frame patch is essential for the 5G and C bands. Subsequently, based on the first antenna model, the second model shown in Figure 3(b) integrates Olympic ring patches into the frame slots, achieving a more uniform current distribution and reducing concentrated current regions, thereby stimulating a resonance at 12.2 GHz. Further optimization of the rectangular frame patches leads to optimized current paths, resulting in better impedance matching and radiation performance within the 4.3 GHz to 8.5 GHz range. Following this, the third model, as
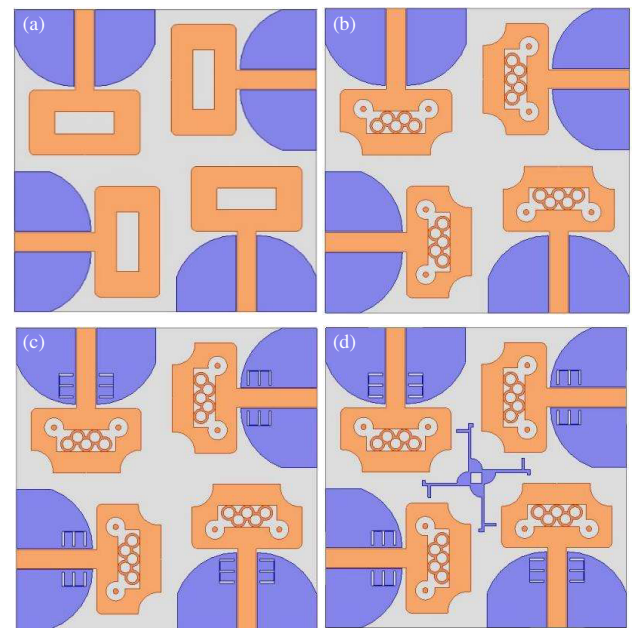

FIGURE 3. Design process of UWB-MIMO antenna: (a) Ant1, (b) Ant2, (c) Ant3, (d) Ant4.

seen in Figure 3(c), involves etching a pair of E-shaped slots on the floor, introducing new current paths and altering the original current flow. The dimensions of the vertical and horizontal slots can be calculated using Equations (1) and (2), where f_c is the resonance frequency of 10.9 GHz, ε_{eff} the effective dielectric constant, ε_r the relative dielectric constant, h the substrate thickness, c the speed of light, and W_g the center conductor width of CPW at 3.5 mm. Continuous refinement of the E-slot design formed specific current distribution patterns, enhancing the resonance effect at 10.9 GHz, improving radiation efficiency, and optimizing the S_{11} parameter, making 9.68 GHz to 11.97 GHz an effective operational band while also increasing port-to-port isolation.

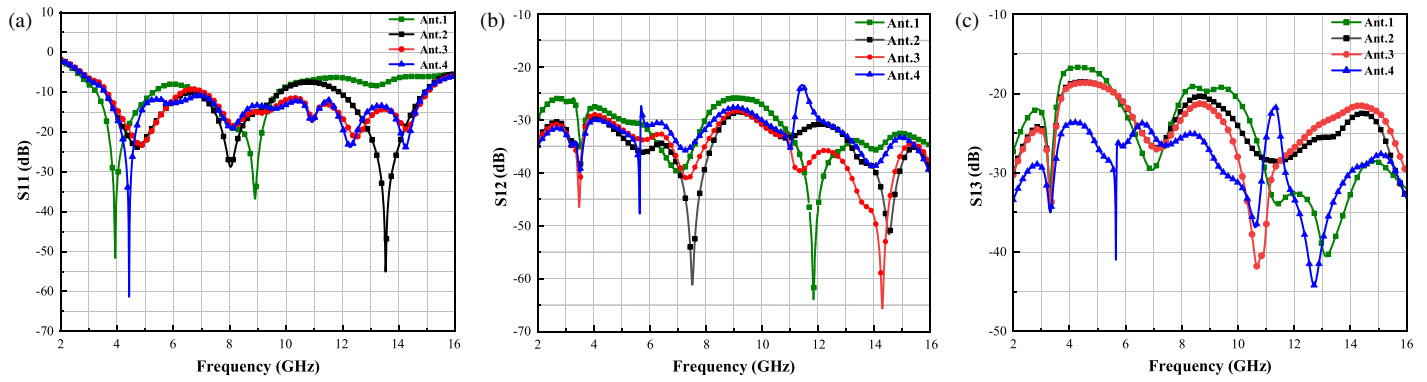$$L_4 = \frac{c}{2f_c\sqrt{\varepsilon_{eff}}} \qquad (1)$$

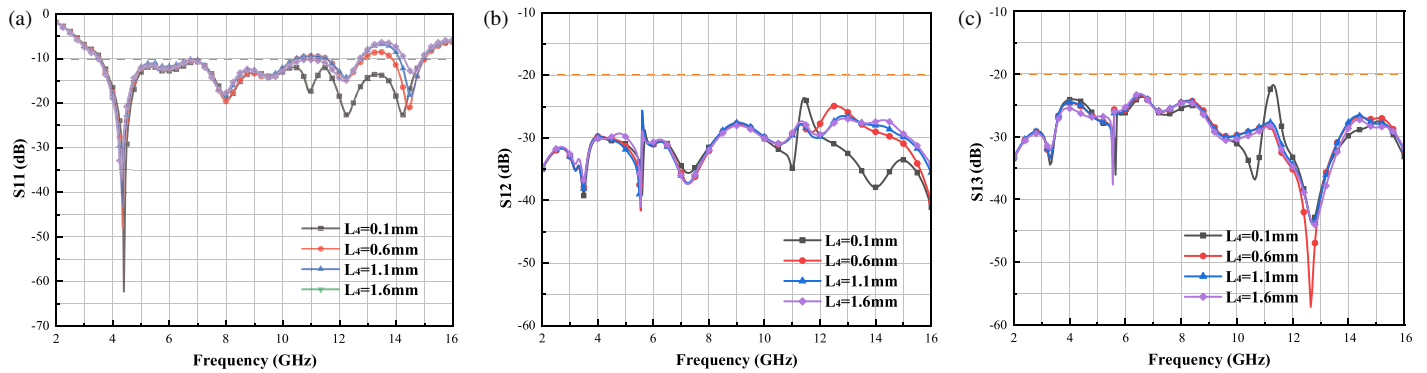**FIGURE 4**. Simulation results for four antennas: (a) S_{11}, (b) S_{12}, (c) S_{13}.

FIGURE 5. Effect of L_4 parameters on antennas S_{11}, S_{12} and S_{13}: (a) S_{11}, (b) S_{12}, (c) S_{13}.

$$\varepsilon_{eff} = 1 + \frac{\varepsilon_r - 1}{2}\left(1 + 12\frac{h}{W_g}\right)^{-\frac{1}{2}} \qquad (2)$$

Finally, the fourth model, Ant4, depicted in Figure 3(d), introduces an innovative windmill-type isolation structure aimed at markedly enhancing the isolation performance between antenna elements. By reducing the current intensity on antenna patches, this configuration effectively minimizes coupling between antennas, with particularly significant effects within the critical 3–6 GHz frequency band. The distinctive design of the windmill isolator not only provides exceptional isolation exceeding 21.7 dB across the entire operational frequency range but also contributes to a substantial expansion of the system's impedance bandwidth. Furthermore, it ensures that the isolation between adjacent antenna elements remains consistently above 21.7 dB throughout the operational bandwidth, thereby significantly enhancing overall communication quality and stability. This advancement paves the way for more robust and reliable antenna system designs.

2.3. Antenna Parameter Analysis

To enhance the performance of UWB-MIMO antennas, this study utilizes high frequency structure simulator (HFSS) software to optimize critical dimensions, adjusting only one parameter at a time to accurately evaluate its impact on antenna performance. This method facilitates a lucid analysis of the sig-

nificance of each design element. Figures 5 and 6 illustrate the optimization process and outcomes, with particular emphasis on the E-shaped slot dimension (L_4) on the fin-shaped ground and the windmill-type isolation structure parameter (M_2), owing to their substantial influence on antenna performance.

As shown in Figure 5(a), reducing the L_4 parameter shifts the resonance point of the antenna towards lower frequencies in the high-frequency band; when L_4 is reduced to 0.1 mm, better impedance matching is achieved within the targeted high-frequency range, along with excellent return loss characteristics at each resonant frequency. From Figures 5(b) and 5(c), it can be observed that changes in the L_4 value have a minor effect on the isolation between antenna ports. However, setting L_4 to 0.1 mm not only achieves good decoupling but also provides a wider operational bandwidth. On the contrary, Figure 6(a) shows that variations in the M_2 parameter do not significantly affect the overall bandwidth of the antenna. However, as illustrated in Figures 6(b) and 6(c), M_2 has a notable impact on port-to-port isolation. As the M_2 dimension decreases, the isolation structure effectively reduces direct electromagnetic coupling paths between antenna elements in the low-frequency band, thereby lowering mutual coupling effects and enhancing isolation at lower frequencies. Nevertheless, in the high-frequency range, reducing the M_2 size alters the resonance mode of the isolation structure, leading to stronger coupling between antenna elements and thus decreasing isolation. Through multiple
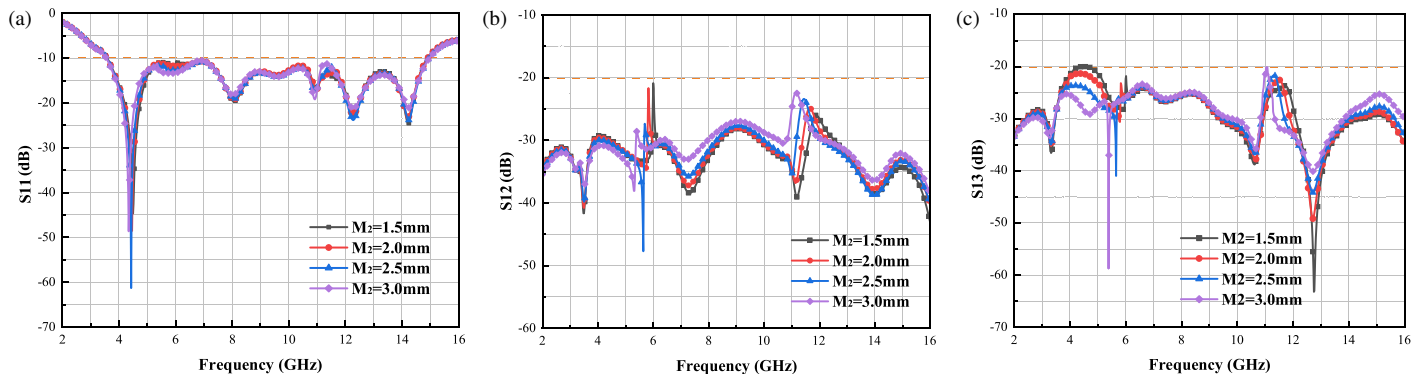
FIGURE 6. Effect of M_2 parameters on antennas S_{11}, S_{12} and S_{13}: (a) S_{11}, (b) S_{12}, (c) S_{13}.

rounds of simulation comparisons, it is determined that setting M_2 to 2.5 mm allows the antenna to achieve both good bandwidth and superior isolation performance.

2.4. Antenna Current Analysis

As depicted in Figure 7(a), the concentration of current in specific regions impedes effective high-frequency resonance. The model illustrated in Figure 7(b) addresses this issue by optimizing the structural design and adjusting the antenna's capacitance and inductance for optimal matching, thereby facilitating high-
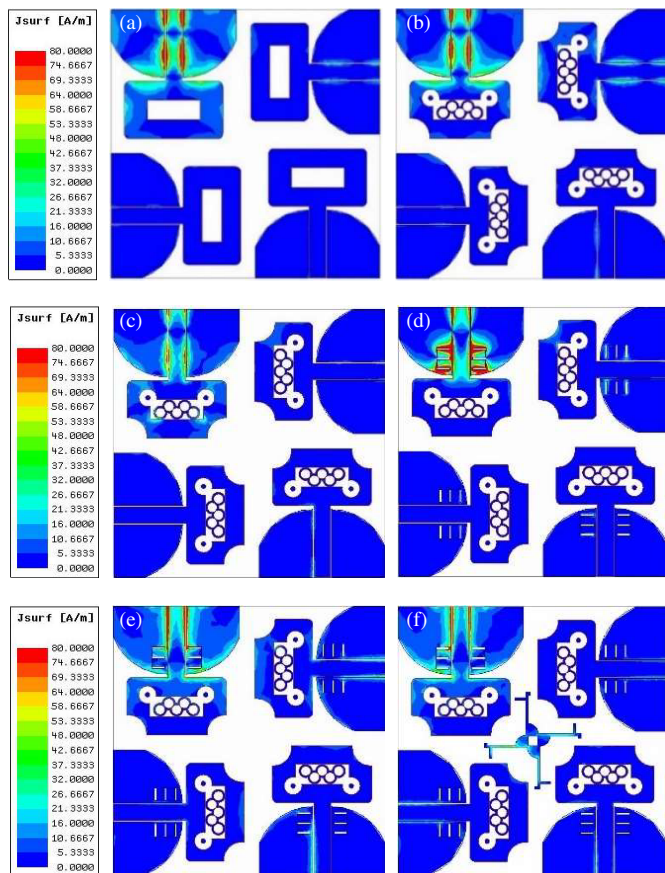

FIGURE 7. Surface current distribution of (a) Ant1 at 13.5 GHz, (b) Ant2 at 13.5 GHz, (c) Ant2 at 10.9 GHz, (d) Ant3 at 10.9 GHz, (e) Ant3 at 5.6 GHz, (f) Ant4 at 5.6 GHz.

frequency resonance. This model also significantly broadens the current distribution area, successfully exciting resonance at 12.2 GHz. Further analysis reveals that strong currents at auxiliary ports under high-frequency conditions enhance the energy and efficiency of the main radiating port through electromagnetic coupling. This enhancement amplifies the resonance effect at the 12.2 GHz frequency point. These improvements not only elevate the overall performance of the antenna but also refine its operational characteristics within critical frequency bands. In the antenna structure shown in Figure 7(c), current predominantly flows along the main body of the antenna, exhibiting a relatively conventional distribution pattern. Due to the absence of specially designed slot structures, this current distribution at specific frequency bands (e.g., 10.9 GHz) results in a high S_{11}, indicating poor impedance matching between the antenna and transmission line, leading to significant energy reflection and a narrow operational bandwidth. In contrast, the antenna model in Figure 7(d) introduces an E-shaped slot on the ground plane based on the structure in Figure 7(c), adding new current paths. This E-shaped slot alters the local electromagnetic environment, inducing currents around the edges of the slot as the current flows through these areas. These induced currents interact with the original currents, significantly altering the current distribution and adjusting the antenna's equivalent impedance. According to the mechanism of how current distribution affects impedance, the new distribution brings the antenna's impedance closer to the characteristic impedance of the transmission line at this frequency band, effectively reducing energy reflection and optimizing the S_{11} parameter. Additionally, the additional current paths introduced by the E-shaped slot enhance the inductive and capacitive effects of the antenna structure, aiding in maintaining good impedance matching performance over a broader frequency range. From the perspective of current intensity, the distribution of current across different frequencies becomes more uniform, no longer concentrated at specific frequency points, thus broadening the antenna's operational bandwidth. In the antenna model shown in Figure 7(e), a novel pinwheel-shaped isolation structure is introduced based on the original layout depicted in Figure 7(f). This design modification alters the spatial structure distribution of the antenna, particularly influencing current paths and distribution at low frequencies. Specifically, the introduction of the pinwheel-shaped isolation structure changes the current flow
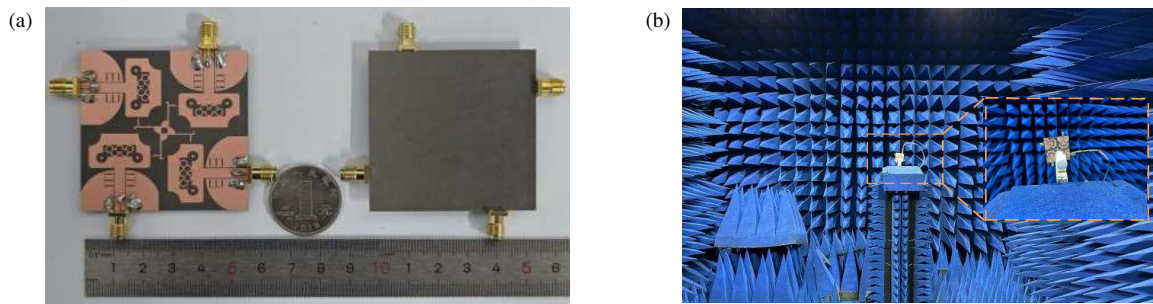
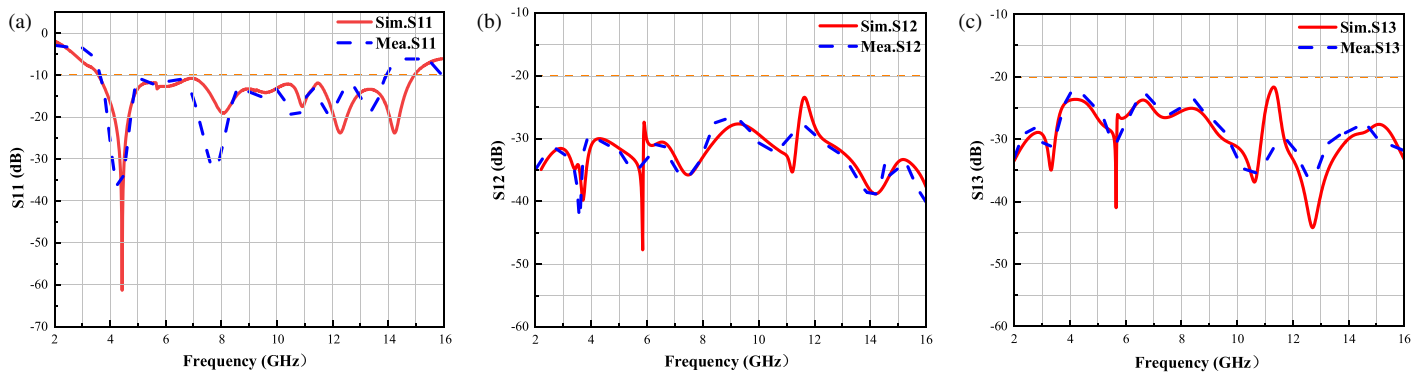**FIGURE 8**. The proposed antenna. (a) Antenna object and (b) antenna microwave darkroom measurement environment.

FIGURE 9. Simulated and measured parameters include S_{11}, S_{12} and S_{13}: (a) S_{11}, (b) S_{12}, (c) S_{13}.

between two ports, effectively disrupting the paths that could cause crosstalk. Moreover, this pinwheel structure redirects portions of the current that would otherwise flow towards adjacent interfering ports, redistributing them into the newly added isolation areas, thereby reducing direct coupling between ports. This optimization notably enhances the isolation between port 1 and port 3. By doing so, it not only minimizes unwanted signal interference but also significantly improves the performance of the antenna system at critical frequency bands, enhancing overall electromagnetic compatibility and signal integrity.

3. RESULTS AND DISCUSSION

3.1. S-Parameters

The MIMO antenna was detailedly simulated using HFSS software, and a prototype was fabricated to verify its practical performance (Figure 8(a)). Performance tests were conducted with an Agilent N52235A vector network analyzer (setup shown in Figure 8(b)). The antenna operates from 3.65 GHz to 13.95 GHz, covering a wide bandwidth. As shown in Figure 9(a), the S_{11} results confirm its broad operational frequency range, while Figures 9(b) and 9(c) illustrate that both S_{12} and S_{13} values remain below -21.7 dB within the UWB spectrum, indicating excellent isolation. Although there are differences between measured and simulated S_{11} and S_{12} values, the overall trends show good consistency, confirming the antenna's performance integrity. These discrepancies are mainly due to manufacturing tolerances, variations in the testing envi-

ronment, and properties of the RO5880 material, but they do not significantly affect the antenna's intended application efficacy.

3.2. Radiation Properties

Radiation patterns of the UWB-MIMO antenna in both the E-plane and H-plane were evaluated in an anechoic chamber at four selected resonant frequencies. The measurement outcomes are depicted in Figure 10. As illustrated in Figure 10(a), at a frequency of 4.45 GHz, the radiation pattern exhibits a classic figure-eight shape with primary lobes directed at 0° and 180°. In the H-plane, both simulated and measured results reveal circular or nearly circular patterns, indicating uniform radiation characteristics across this plane. Figure 10(b) presents the scenario at 8.1 GHz, where the E-plane shows prominent main lobes (indicating maximum radiation) at 0° and 180°, while the H-plane displays significant lobes at 90° and 270°, highlighting the strongest radiation directions for the antenna. According to Figure 10(c), at 10.925 GHz, the primary lobe orientations for the E-plane and H-plane are located at 0°, 180° and 90°, 70°, respectively. Finally, Figure 10(d) indicates that at 12.285 GHz, the main lobe in the E-plane remains at 0° and 180°, whereas in the H-plane, it is situated at 90° and 270°.

Figure 11 illustrates the peak gain and radiation efficiency of the MIMO antenna, with a maximum gain reaching 7.2 dBi and radiation efficiency ranging from 87% to 93%. Within the frequency range of 3.65 GHz to 13.95 GHz, the radiation efficiency exceeds 87%, indicating that the antenna effectively radiates most of the input energy, showcasing its outstanding performance. These results confirm the antenna's efficient energy
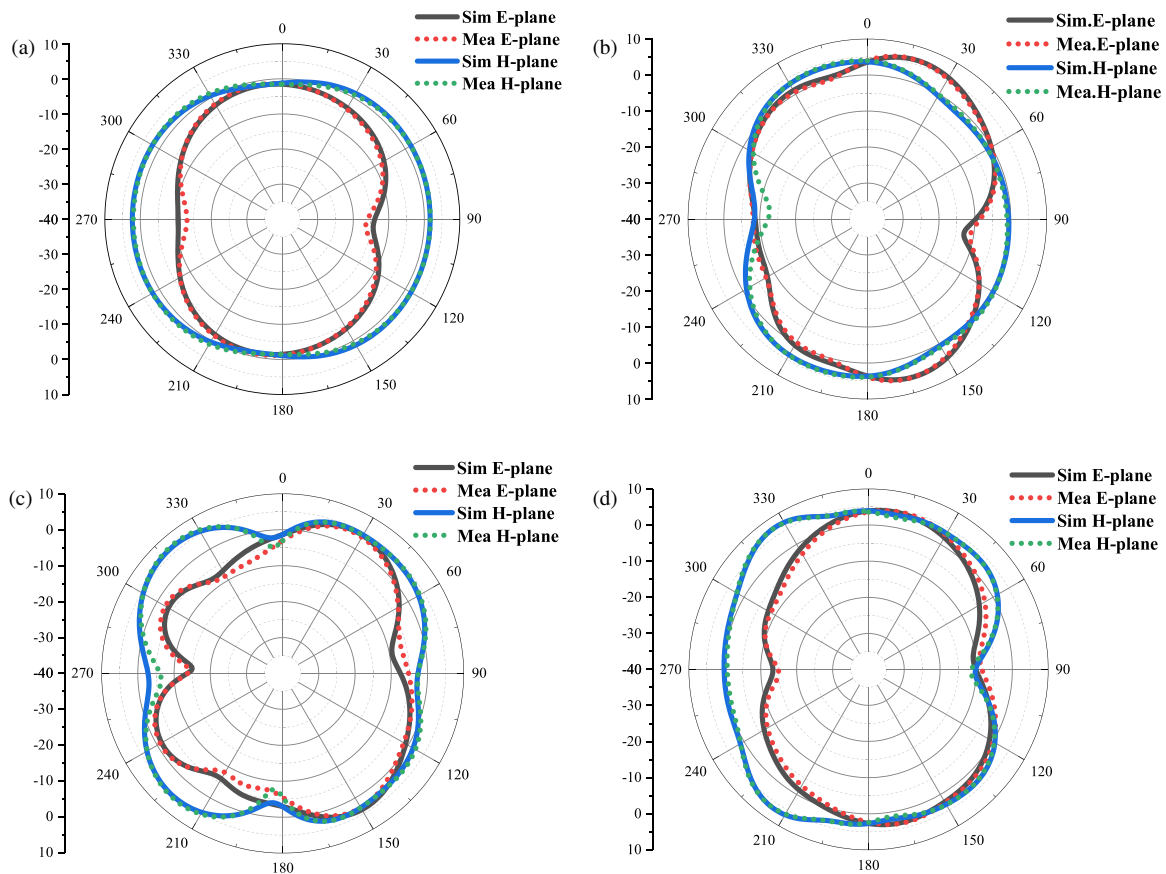
FIGURE 10. Simulated and measured orientation diagrams: (a) 4.45 GHz, (b) 8.1 GHz, (c) 10.925 GHz, (d) 12.285 GHz.
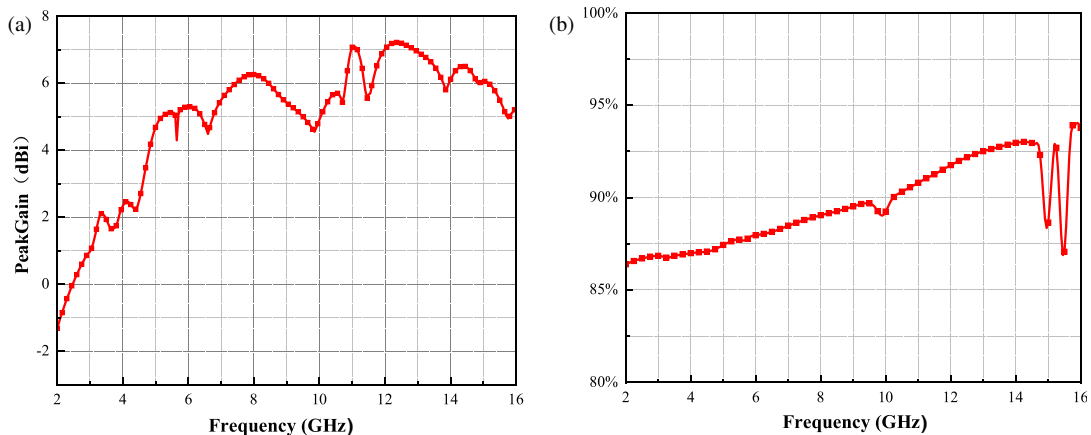

FIGURE 11. Peak gain and radiation efficiency of the antenna: (a) Peak gain, (b) radiation efficiency.

conversion capability and overall reliability within this band, and its stability across the entire wideband makes it an ideal choice for high-efficiency broadband applications.

3.3. MIMO Antennas Performance

3.3.1. ECC and TARC

ECC evaluates the signal correlation between antenna elements in a MIMO system, serving as a critical metric for assessing di-

versity capability and coupling effects. A lower ECC indicates reduced mutual interference and superior system performance, with ECC typically required to be below 0.5. Orthogonal layout ensures that adjacent antennas have orthogonally polarized electromagnetic fields, reducing overlap in radiation patterns and signal correlation, thereby ensuring independent propagation paths for electromagnetic waves. In scenarios of multipath fading, the correlation of signals received at different orthogonal ports is significantly reduced, directly lowering the ECC value. This approach optimizes the overall performance of the
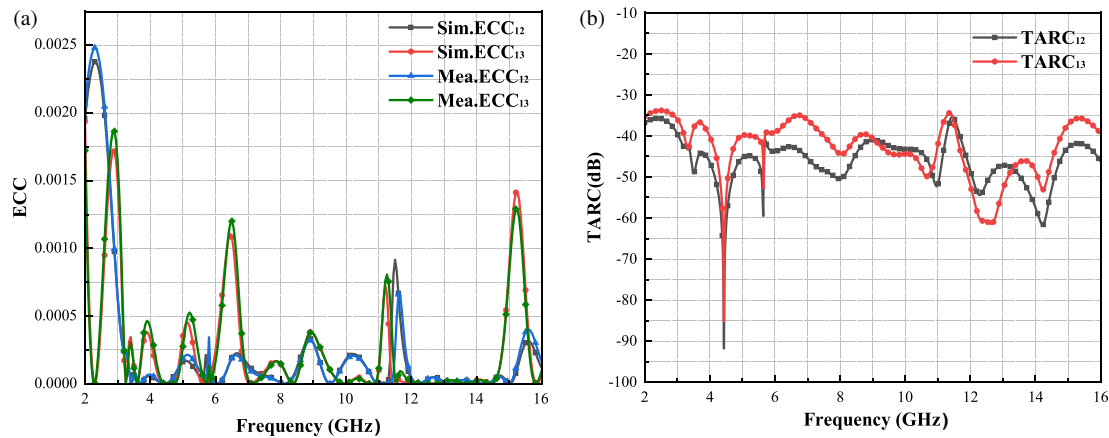
FIGURE 12. ECC and TARC of the antenna: (a) ECC, (b) TARC.

TABLE 2. Comparison of the proposed antenna with several existing antennas.

Ref.	Size (mm^2)	Bandwidth (GHz)	Isolation (dB)	ECC	Radiation efficiency (%)
[11]	$1.2\lambda \times 0.6\lambda$	2.3–11.5	> 16	< 0.0012	-
[12]	$0.9\lambda \times 0.9\lambda$	3.4–12.2	> 18	< 0.006	-
[20]	$2.2\lambda \times 2.2\lambda$	2.77–12	> 15	< 0.1	75–85
[21]	$0.67\lambda \times 0.81\lambda$	3.89–17.09	> 15	< 0.02	89
[22]	$1.2\lambda \times 1.75\lambda$	2.92–16.97	> 19	< 0.005	73-96
[23]	$0.85\lambda \times 1.5\lambda$	3.05–13.38	> 17	< 0.007	89–97
[24]	$1.6\lambda \times 1.6\lambda$	4.6–16.4	> 20	< 0.002	85–93
[25]	$1.02\lambda \times 0.61\lambda$	4.8–15.63	> 20	< 0.0075	75–82
[26]	$0.54\lambda \times 0.54\lambda$	2.9–10.6	> 15	< 0.01	-
This work	$1.5\lambda \times 1.5\lambda$	3.65–13.95	> 21.7	< 0.0012	87–93

antenna system, with measured and simulated results shown in Figure 12(a). The specific formula for calculating ECC is as follows:

$$\text{ECC} = \frac{\left| S_{ii}^* S_{ij} + S_{ji}^* S_{jj} \right|^2}{\left(1 - |S_{ii}|^2 - |S_{ji}|^2 \right) \left(1 - |S_{jj}|^2 - |S_{ji}|^2 \right)} \quad (3)$$

In MIMO systems, mutual and self-impedances significantly affect antenna radiation performance, making it insufficient to evaluate the system by analyzing individual S-parameters alone. TARC values capture these impedance changes, offering insights into system behavior; a TARC below -10 dB indicates good antenna performance. Monitoring TARC helps understand antenna interactions and overall system performance. Orthogonal distribution minimizes electromagnetic coupling and reflected signal overlap by orienting adjacent antenna elements perpendicularly, achieving orthogonal radiation patterns. This approach, enhanced by polarization isolation and structural decoupling, reduces reflection coupling and impedance mismatches, keeping TARC values below -30 dB as shown in Figure 12(b). It provides a low-reflection, high-matching hardware foundation for reliable MIMO communications, with spe-

cific values derived from Equation (4):

$$\text{TARC}_{ij} = \sqrt{\frac{(S_{ii} + S_{ij})^2 + (S_{ji} + S_{jj})^2}{2}} \quad (4)$$

4. COMPARE WITH EXISTING ANTENNAS

Table 2 provides a comparative analysis of the proposed antenna and several existing antennas in terms of key performance metrics such as size, operational bandwidth, isolation, ECC, and radiation efficiency. Compared to the design in [20], the proposed antenna achieves a more compact structure, and compared to the 1440 mm^2 dual-port diversity structure in [27], this represents a reduction of 45.6%. Compared with antennas from [11, 12, 20, 26, 28], the proposed antenna exhibits a broader operational bandwidth and superior signal isolation compared to those discussed in [11, 12, 20–27, 29]. Additionally, the ECC value of the proposed antenna is lower than that of the antennas mentioned in [12, 20, 21–29]. Furthermore, the proposed antenna boasts an excellent radiation efficiency over 87%. Considering all these advantages, it can be concluded that the proposed antenna demonstrates superior overall performance, fully meeting the design standards and requirements

for UWB-MIMO antennas. The novelty of this design lies in achieving multiple performance breakthroughs through simple geometric structures, balancing ultra-wideband, high isolation, and low correlation within a compact size without relying on complex decoupling elements or multi-layer substrates.

5. CONCLUSION

This study proposes a high-isolation UWB-MIMO antenna system suitable for various applications such as UWB IoT devices, precise positioning services for smartphones and wearable devices, vehicular networking, and autonomous driving assistance systems. When the antenna is placed in the middle of the printed circuit board (PCB), a layered design approach can be adopted, placing the antenna on the top layer of the PCB while situating other circuits on the bottom or inner layers, using substrate materials like Rogers RO5880 to minimize inter-layer coupling. CPW feeding technology, due to its compact structure, reduces interference with surrounding circuits, facilitating integration. Optimizing a single antenna system is crucial for multi-antenna designs, especially under space and budget constraints. To achieve massive MIMO, the "Olympic-ring patch and windmill-shaped decoupling" units can be replicated to form 8×8 or 16×16 arrays. This system achieves port isolation exceeding 21.7 dB, bandwidth coverage from 3.65 GHz to 13.95 GHz, radiation efficiency between 87% and 93%, ECC less than 0.0012, and TARC below -30 dB, demonstrating low correlation and excellent performance in independent channel operation. Therefore, this antenna is highly suitable for next-generation massive MIMO systems, although further optimization in beamforming technology and compact integration remains necessary.

REFERENCES

[1] Shome, P. P., T. Khan, A. A. Kishk, and Y. M. M. Antar, "Quad-element MIMO antenna system using half-cut miniaturized UWB antenna for IoT-based smart home digital entertainment network," *IEEE Internet of Things Journal*, Vol. 10, No. 20, 17 964–17 976, 2023.

[2] Tripathi, S., A. Mohan, and S. Yadav, "A compact octagonal fractal UWB MIMO antenna with WLAN band-rejection," *Microwave and Optical Technology Letters*, Vol. 57, No. 8, 1919–1925, 2015.

[3] Wu, L., X. Cao, and B. Yang, "Design and analysis of a compact UWB-MIMO antenna with four notched bands," *Progress In Electromagnetics Research M*, Vol. 108, 127–137, 2022.

[4] Shailesh, G. S., S. Kumar, S. I. Alshathri, W. El-Shafai, and O. P. Kumar, "Compact UWB MIMO antenna with a modified back reflector and supported by characteristic mode analysis for wireless communication applications," *IEEE Access*, Vol. 12, 187 302–187 312, 2024.

[5] Naidu, P. R. T., C. Saha, K. V. Krishna, L. A. Shaik, J. Y. Siddiqui, and Y. Antar, "Compact multiple EBG cells loaded UWB-narrowband antenna pair with high isolation for cognitive radio (CR) based MIMO applications," *AEU — International Journal of Electronics and Communications*, Vol. 127, 153420, 2020.

[6] Wang, E., W. Wang, X. Tan, Y. Wu, J. Gao, and Y. Liu, "A UWB MIMO slot antenna using defected ground structures for high isolation," *International Journal of RF and Microwave Computer-Aided Engineering*, Vol. 30, No. 5, e22155, 2020.

[7] Alharbi, A. G., U. Rafique, S. Ullah, S. Khan, S. M. Abbas, E. M. Ali, M. Alibakhshikenari, and M. Dalarsson, "Novel MIMO antenna system for ultra wideband applications," *Applied Sciences*, Vol. 12, No. 7, 3684, 2022.

[8] Rafique, U., S. Pisa, R. Cicchetti, O. Testa, and M. Cavagnaro, "Ultra-wideband antennas for biomedical imaging applications: A survey," *Sensors*, Vol. 22, No. 9, 3230, 2022.

[9] Agarwal, S., U. Rafique, R. Ullah, S. Ullah, S. Khan, and M. Donelli, "Double overt-leaf shaped CPW-fed four port UWB MIMO antenna," *Electronics*, Vol. 10, No. 24, 3140, 2021.

[10] Tahir, M. U., U. Rafique, and M. M. Ahmed, "Rhombus-inscribed circular ring fractal array antenna for millimeter-wave 5G applications," *International Journal of Antennas and Propagation*, Vol. 2022, No. 1, 8254785, 2022.

[11] Kiani, S. H., H. S. Savci, M. E. Munir, A. Sedik, and H. Mostafa, "An ultra-wide band MIMO antenna system with enhanced isolation for microwave imaging applications," *Micromachines*, Vol. 14, No. 9, 1732, 2023.

[12] Lu, Z., H. Lin, Z. Wang, W. Nie, and W. Mu, "Compact ACS-fed MIMO antenna with dual-band notch characteristics for UWB applications," *International Journal of Microwave and Wireless Technologies*, Vol. 16, No. 3, 478–486, 2024.

[13] Addepalli, T., K. V. Babu, T. Vidyavathi, R. Manda, and B. K. Kumar, "Design and analysis of nonagonal patch unite with rectangular shaped 4-element UWB-MIMO antenna for portable wireless device applications," *Analog Integrated Circuits and Signal Processing*, Vol. 114, No. 3, 459–473, 2023.

[14] Khan, A., S. Bashir, S. Ghafoor, H. Rmili, J. Mirza, and A. Ahmad, "Isolation enhancement in a compact four-element MIMO antenna for ultra-wideband applications," *Computers, Materials & Continua*, Vol. 75, No. 1, 911–925, 2023.

[15] Liu, F., J. Guo, L. Zhao, G.-L. Huang, Y. Li, and Y. Yin, "Dual-band metasurface-based decoupling method for two closely packed dual-band antennas," *IEEE Transactions on Antennas and Propagation*, Vol. 68, No. 1, 552–557, 2020.

[16] Fadehan, G. A., Y. O. Olasoji, and K. B. Adedeji, "Mutual coupling effect and reduction method with modified electromagnetic band gap in UWB MIMO antenna," *Applied Sciences*, Vol. 12, No. 23, 12358, 2022.

[17] Mathur, R. and S. Dwari, "Compact planar reconfigurable UWB-MIMO antenna with on-demand worldwide interoperability for microwave access/wireless local area network rejection," *IET Microwaves, Antennas & Propagation*, Vol. 13, No. 10, 1684–1689, 2019.

[18] Wang, L., Z. Du, H. Yang, R. Ma, Y. Zhao, X. Cui, and X. Xi, "Compact UWB MIMO antenna with high isolation using fence-type decoupling structure," *IEEE Antennas and Wireless Propagation Letters*, Vol. 18, No. 8, 1641–1645, 2019.

[19] Hosain, M. M., S. Kumari, and A. K. Tiwary, "Sunflower shaped fractal filtenna for WLAN and ARN application," *Microwave and Optical Technology Letters*, Vol. 62, No. 1, 346–354, 2020.

[20] Ahmed, B. T., "High isolation compact UWB MIMO antennas," *Wireless Personal Communications*, Vol. 128, No. 4, 3003–3029, 2023.

[21] Desai, J. K., M. M. Kamruzzaman, S. Hubálovský, H.-T. Hsu, and A. A. Ibrahim, "Interconnected CPW fed flexible 4-port MIMO antenna for UWB, X, and Ku band applications," *IEEE Access*, Vol. 10, 57 641–57 654, 2022.

[22] Yao, S., X. Qiu, and T. Yang, "A miniaturized UWB MIMO antenna design for 5G multi-band applications," *Progress In Electromagnetics Research C*, Vol. 153, 1–12, 2025.

[23] Yao, S., T. Yang, X. Qiu, and X. Li, "A frog-shaped UWB MIMO antenna design for 5G," *Progress In Electromagnetics Research C*, Vol. 151, 101–112, 2024.

[24] Kumar, P., S. Pathan, S. Vincent, O. P. Kumar, P. Kumar, P. R. Shetty, T. Ali, *et al.*, "A compact quad-port UWB MIMO antenna with improved isolation using a novel mesh-like decoupling structure and unique DGS," *IEEE Transactions on Circuits and Systems II: Express Briefs*, Vol. 70, No. 3, 949–953, 2023.

[25] Mu, W., H. Lin, Z. Wang, C. Li, M. Yang, W. Nie, and J. Wu, "A flower-shaped miniaturized UWB-MIMO antenna with high isolation," *Electronics*, Vol. 11, No. 14, 2190, 2022.

[26] Dhanalakshmi, K. M. and S. Rajkumar, "A monopole polarisation diversity antenna for high density packaging MIMO applications," *Microelectronics International*, Vol. 41, No. 2, 75–81, 2024.

[27] Jaglan, N., S. D. Gupta, E. Thakur, D. Kumar, B. K. Kanaujia, and S. Srivastava, "Triple band notched mushroom and uniplanar EBG structures based UWB MIMO/diversity antenna with enhanced wide band isolation," *AEU — International Journal of Electronics and Communications*, Vol. 90, 36–44, 2018.

[28] Jaglan, N., S. D. Gupta, B. K. Kanaujia, and M. S. Sharawi, "10 element sub-6-GHz multi-band double-T based MIMO antenna system for 5G smartphones," *IEEE Access*, Vol. 9, 118 662–118 672, 2021.

[29] Jaglan, N., S. D. Gupta, and M. S. Sharawi, "18 element massive MIMO/diversity 5G smartphones antenna design for sub-6 GHz LTE bands 42/43 applications," *IEEE Open Journal of Antennas and Propagation*, Vol. 2, 533–545, 2021.